ADVANCED ENERGY MATERIALS
www.advenergymat.de

Printing High-Quality Formanidinum Lead Triiodide Films: Understanding the Critical Role of α-Phase Nucleation Before Thermal Annealing

Shudi Qiu, Lirong Dong, Dongju Jang, Fu Yang, José Garcia Cerrillo, Chaohui Li, Zhiqiang Xie, Junsheng Luo, Fei Guo, Andreas Distler, Tian Du, Christoph J. Brabec,* and Hans-Joachim Egelhaaf*

Upscaling the coating of formamidinium lead triiodide ($FAPbI_3$) thin film is essential to realizing full printing and thereby roll-to-roll production of perovskite photovoltaics. However, thin-film $FAPbI_3$ processed from antisolvent-free, printing methods suffer from undesirable degradation to the non-photoactive phase, particularly in ambient processing conditions. Here, the most critical stage in thin-film processing is identified as the gas-quenching treatment of the as-cast wet film. It is crucial to achieve both the nucleation of α-phase nanocrystals and their sufficient growth at room temperature, which are indispensable for templating the growth of a highly crystalline and stable α-$FAPbI_3$ film during subsequent thermal annealing. The gas-quenching-treated film without these α-phase nanocrystals can only be converted to meta-stable α-$FAPbI_3$ by thermal annealing. By precisely identifying the spontaneous doping of cesium ion (Cs^+) as a key factor in triggering α-$FAPbI_3$ nucleation and the role of chloride ion (Cl^-) in enhancing nanocrystal growth, a generalized mechanism for additive engineering for the precursor ink is theorized. The identified mechanism translates to a power conversion efficiency of 19.36% for fully printed carbon-electrode solar cells, 16.23% for carbon-electrode minimodules, and excellent operational stability, showing the promising potential of this proposed fabrication route in the upscaling of perovskite photovoltaics.

1. Introduction

Formamidinium lead triiodide ($FAPbI_3$) has gained significant attention as the light absorber in perovskite solar cells (PSCs) owing to its bandgap close to the Shockley-Queisser optimum and superior thermal stability compared to the conventional methylammonium (MA^+)-based counterparts.[1,2] However, compared to Cs^+ (1.67 Å) and MA^+ (2.17 Å), the larger size of FA^+ (2.53 Å) results in the Goldschmidt tolerance factor (t) exceeding the upper limit of the ideal range, which is between 0.9 and 1.0, for perovskite structure formation.[3–5] Consequently, the photoactive α-$FAPbI_3$ is prone to transformation to a photo-inactive, non-perovskite δ-$FAPbI_3$ in ambient conditions.[6,7] The presence of the photoinactive δ phase not only undermines the photovoltaic performance of PSCs, but also accelerates film degradation by further triggering the transition of the adjacent α phase into the δ phase.[6,8] Owing to lower

S. Qiu, L. Dong, D. Jang, J. G. Cerrillo, C. Li, Z. Xie, J. Luo, A. Distler, T. Du, C. J. Brabec, H.-J. Egelhaaf
Institute of Materials for Electronics and Energy Technology (i-MEET)
Department of Materials Science and Engineering
Friedrich-Alexander-Universität Erlangen-Nürnberg
Martensstraße 7, 91058 Erlangen, Germany
E-mail: tian.du@fau.de; christoph.brabec@fau.de

The ORCID identification number(s) for the author(s) of this article can be found under https://doi.org/10.1002/aenm.202402616

DOI: 10.1002/aenm.202402616

F. Yang
Laboratory of Advanced Optoelectronic Materials
Suzhou Key Laboratory of Novel Semiconductor-optoelectronics Materials and Devices
College of Chemistry
Chemical Engineering and Materials Science
Soochow University
Suzhou 215123, China

F. Guo
Institute of New Energy Technology
College of Information Science and Technology
Jinan University
Guangzhou 510632, China

T. Du, C. J. Brabec, H.-J. Egelhaaf
Helmholtz Institute Erlangen-Nürnberg for Renewable Energy (HIERN)
Forschungszentrum Jülich
Immerwahrstraße 2, 91058 Erlangen, Germany

formation enthalpy of δ-$FAPbI_3$ at room temperature,[9] it remains difficult to grow high-quality, stable and phase-pure α-$FAPbI_3$ thin films without any residual δ phase. This is an issue already for research cells manufactured in glove box environments, but becomes a critical challenge in the production of large-area perovskite modules by printing under ambient conditions. Tackling this challenge to provide robust solutions for high-throughput production of perovskite PV is the overall goal of this study.

A variety of strategies has been developed to obtain $FAPbI_3$ of pure α-phase,[10–14] among which commonly used are compositional engineering of $FAPbI_3$ and additive engineering of the precursor solution. Compositional engineering involves alloying $FAPbI_3$ with smaller-sized cations including MA^+, Cs^+,[15] or halide such as bromide (Br^-), that form the widely used "mix-cation mix-halides" perovskites.[16–19] However, this strategy leads to an undesired increase of the perovskite bandgap, as well as likely segregation of Br-rich phases.[9] In this regard, a trace amount of halide additives to the solution containing stoichiometric $FAPbI_3$is shown to produce highly crystalline,[20–22] phase-pure α-$FAPbI_3$ films with no significant increase of bandgap or no noticeable phase segregation observed. However, most of the highly efficient PSCs were fabricated by spin-coating in an N_2 glove box,[23] whereas upscaling the processing of α-$FAPbI_3$ films with industrial printing techniques on large areas requires a robust and reliable processing recipe.[24–27] While roll-to-roll printing has been demonstrated as one of the most promising processes for perovskite photovoltaic application,[28] the perovskite ink currently is based on MA-dominant perovskites. It remains unclear whether the processing recipes developed based on the spin-coating technique are directly transferrable to the printing technique, which hinders the upscaling of $FAPbI_3$ thin films and photovoltaics. It is imperative to deepen our understanding film formation mechanism, particularly the key processes governing the high crystallinity and stability of α-$FAPbI_3$, before we can faithfully transfer or adapt the developed processing recipes in printing techniques, which is the motivation for this work.

In this work, we investigated the key crystallization mechanism toward highly crystalline and stable α-$FAPbI_3$ in the course of scalable, gas-quenching-assisted printing fabrication, unraveling the drying of the as-cast wet film by airflow (the so-called "gas quenching") prior to thermal annealing to be the most critical stage in governing film quality. With in-situ spectroscopic techniques, we not only elucidated the formation of α-phase perovskites during gas-quenching treatment to be indispensable in obtaining highly crystalline, stable α-$FAPbI_3$ film growth in the subsequent thermal annealing, but also identified the key ionic species involving in these processes. A universal, reliable strategy based on chlorinated additives to the precursor ink was therefore derived from our investigations, enabling the printing of high-quality α-$FAPbI_3$ film, which translates to a power conversion efficiencies (PCE) of 19.36% for fully printed carbon-electrode perovskite solar cells (C-PSCs), 16.23% for carbon-electrode perovskite minimodules (C-PSMs), as well as excellent operational stability under 1 Sun, 65 °C aging test for unencapsulated devices in N_2 and damp heat testing (85% RH, 85 °C) for encapsulated devices. This work provides a fundamental and unique perspective toward understanding the fabrication of α-$FAPbI_3$ for efficient, stable, and fully printed perovskite photovoltaic devices.

2. Results and Discussion

2.1. Impact of Processing Additives on the Formation of α-$FAPbI_3$

To investigate the critical factors in obtaining highly crystalline and stable α-$FAPbI_3$ film, we start with modifying the thin-film crystallization kinetics by modulating the stoichiometric $FAPbI_3$ composition in precursor solution with different alkali metal chlorides or organochlorides additives (in all cases, the additive concentration is 10% $_{mol}$), including guanidinium chloride (GaCl), formamidinium chloride (FACl), cesium chloride (CsCl), methylammonium chloride (MACl) and potassium chloride (KCl). The cations from the additive species differ in ionic radius of FA^+ (Table S1, Supporting Information), they are able to tune the Goldschmidt tolerance factor of the perovskite structure. These precursor inks are blade coated onto the substrate, the wet films are then dried by a continuous stream of dry air, the so-called "gas quenching" treatment, prior to thermal annealing at 150 °C for 10 min to obtain crystalline films. Gas quenching is arguably the most widely used method in the printing of perovskite, essential to the fabrication of a smooth, compact, and pinhole-free film.[29] We show a video in supporting information (Video S1, Supporting Information) demonstrating the gas-quenching-assisted printing process, and in Figure S1 (Supporting Information) that a minimum gas pressure of 1.5 bar is required to ensure film compactness.

In **Figure 1a**, the change to film crystallization can be immediately seen from the photographs of the perovskite films, taken after gas quenching but prior to thermal annealing (upper panel), taken after thermal annealing (middle panel), and taken after storing in the air for 30 min (bottom panel), respectively. It is obvious that after gas quenching treatment, a brownish film is only obtained when CsCl is added, whilst other films remain yellowish and transparent. All films turn black during thermal annealing at 150 °C, but they convert back to a transparent yellow color after having cooled down and being stored in an ambient atmosphere at room temperature for approximately 30 min, except for the film containing CsCl that remains black. The observation of black films upon annealing can be ascribed to the well-known fact that the phase transition from δ- to α- $FAPbI_3$ typically requires high temperatures.

The X-ray diffraction (XRD) pattern of a gas-quenched film prior to thermal annealing, Figure 1b, shows a mixture of non-perovskite δ-$FAPbI_3$ (peak at 11.7°) and intermediate phases (peaks emerging at 6.68° and 9.20°) for $FAPbI_3$ films without additives.[30–32] However, it is clear that by adding MACl, FACl, and CsCl to the precursor ink, a small amount of α-$FAPbI_3$ (characteristic peak at 14.1°) is observed after gas-quenching. The XRD pattern of the annealed films, Figure 1c, shows that pure α-$FAPbI_3$ can be obtained only in the case of CsCl and MACl being used as additives, despite that the film with CsCl exhibits higher crystallinity compared to that with MACl. In all other cases, there is a co-existence of α-$FAPbI_3$ and δ-$FAPbI_3$, and a quantification of the peak area of δ-phase and α-phase in the films is shown in Figure S2 (Supporting Information). The results highlight an issue that only when the gas-quenched film contains a certain critical amount of α-$FAPbI_3$, a complete conversion of the film to α-$FAPbI_3$ can be achieved by thermal annealing. This critical amount of α-$FAPbI_3$ in the gas-quenched film can only be

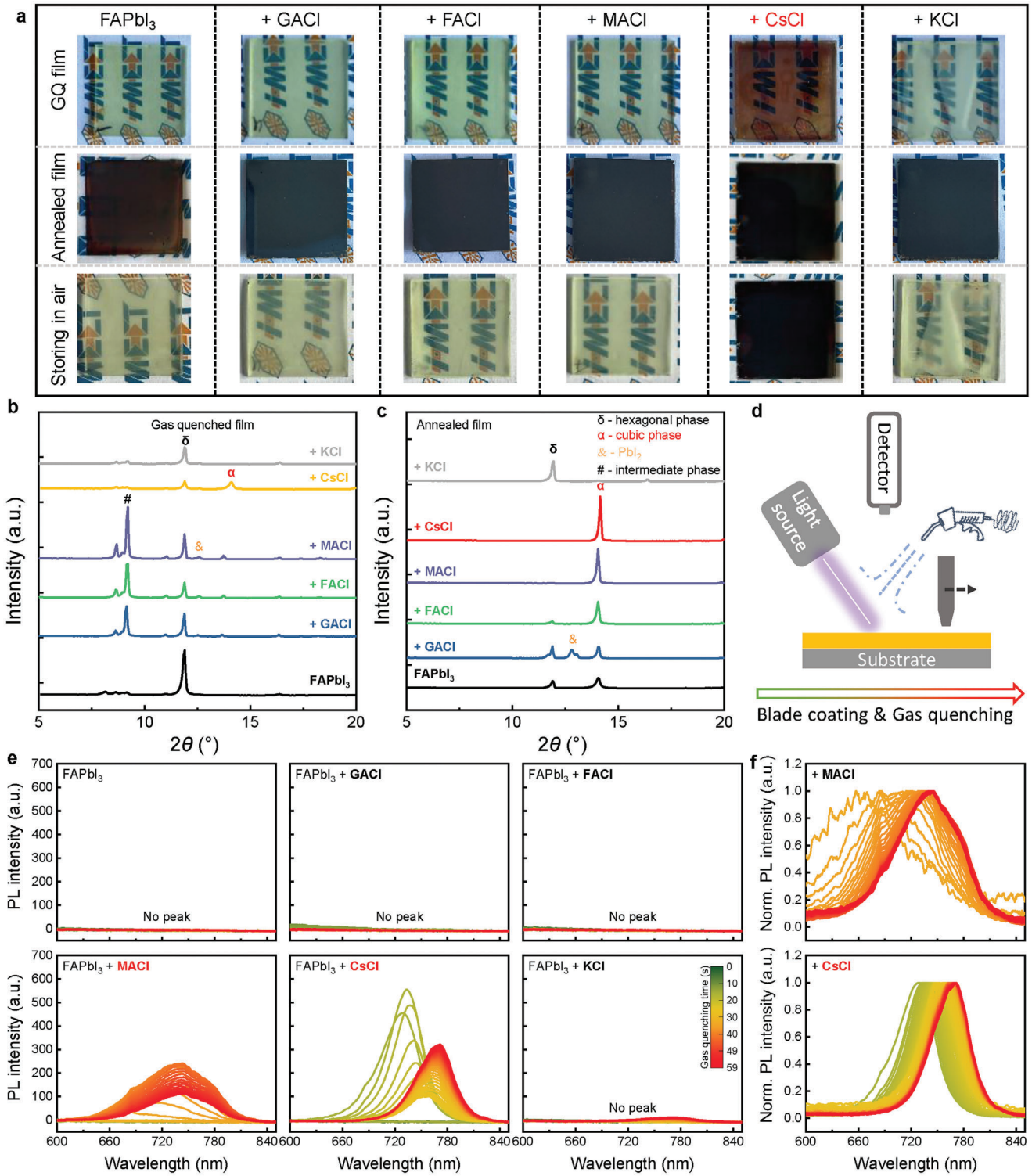

Figure 1. The role of processing additives on the formation of α-$FAPbI_3$. a) Photographs of $FAPbI_3$ perovskite films processed from precursor inks containing different alkali metal chloride or organochloride additives, taken at different processing stages: after gas quenching for 1 min (top panel), after thermal annealing at 150 °C for 10 min (middle panel) and after storing in ambient air of 30–40% RH for 30 min (bottom panel). b) XRD patterns of the gas-quenched films processed from additives. c) XRD patterns of films right after 150 °C thermal annealing. d) Schematic illustration of the in-situ PL and UV–vis absorption measurement during gas quenching treatment of the wet films. e) Evolution of the PL spectra of $FAPbI_3$ films processed with different additives during gas quenching treatment. f) Normalized in-situ PL spectra during gas quenching treatment.

achieved by adding MA and Cs, as they bring the system back to a lower Goldschmidt factor. Meanwhile, the varying stabilities of the two cases suggest differences in either the crystallization pathways or final crystal structures (Figure 1a). The inferior stability observed when using MACl is likely attributable to atmospheric humidity[33] and the lower sublimation temperature of MA compared to FA during high-temperature annealing, with boiling points of −6.3 and 46.3 °C, respectively.[34]

We then turn to investigate the emergence of α-$FAPbI_3$ during the gas-quenching stage, that is, before thermal annealing, using in-situ photoluminescence (PL) and UV–vis absorption spectroscopies. The spectrometers are built alongside the blade coater, Figure 1d, for continuous inspection of the as-cast films during their drying. In Figure 1e we plot the evolution of PL measured from the wet films during the implementation of gas quenching. PL peaks are only seen in films with MACl and CsCl as additives, indicating the emergence of the photoactive perovskite phase, namely α-$FAPbI_3$. In all other cases, no noticeable PL can be observed, suggesting that the films are dominated by non-perovskite phases, i.e., intermediate phase and/or δ-$FAPbI_3$. The emergence of perovskite phase in the case of CsCl or MACl additive is also confirmed by fluorescence microscopic images taken during gas quenching, Figure S3 (Supporting Information).

To probe the spectral evolution in more detail we plot the normalized spectra for films with MACl and CsCl in Figure 1f. The PL signals in both cases emerge from a shorter wavelength (720–740 nm) but continuously shift toward a longer wavelength as gas quenching goes on. Such observation is ascribed to an effect of size increase of the perovskite nanocrystals, suggesting the nucleation of α-$FAPbI_3$ type perovskite from the liquid phase and subsequent growth of these nanocrystals, consistent with the XRD pattern that shows the diffraction peak of α-$FAPbI_3$. The intensity of PL, in both cases, rises sharply at the beginning of gas quenching but is followed by a decrease at the later stage. This can be explained by the fact that the nanocrystals are most luminescent in the state of quantum dots but become less luminescent as the nanocrystals grow and thus comprise an increasing number of defects, e.g., the boundaries with surrounding nanocrystals and that PL quenching by these defects overwhelms the PL enhancement by the increased volume of crystalline perovskite.[35–38] The formation of the crystalline perovskite phase can be further evidenced by the evolution of the in-situ absorption spectra during gas quenching, Figure S4 (Supporting Information). The wet films processed with MACl or CsCl additives show progressively increased absorbance with a clear absorption onset observed at ≈800 nm. These observations indicate that gas quenching drives the nucleation of α-$FAPbI_3$ and the growth of the nanocrystals by adding MACl or CsCl to the precursor ink.

A detailed comparison of the spectral evolution of PL between MACl and CsCl shows overall higher PL intensity (Figure 1e) and a more uniform pace of PL peak shift (Figure 1f) for CsCl than for MACl. The spectra of films with CsCl additive also demonstrate a narrower and more symmetric PL peak and a larger peak shift toward higher wavelengths from the beginning to the end of gas quenching (Figure 1f). These observations indicate that both CsCl and MACl drive the nucleation of α-$FAPbI_3$, but CsCl outperforms MACl by inducing a higher nucleation density and accelerating the growth of the nuclei. These differences result in the formation of larger α-$FAPbI_3$ crystals with relatively narrow size distribution at the end of gas quenching.

In parallel to the nucleation of α-phase perovskite in the case of CsCl or MACl additive, the in-situ absorption spectra suggest the nucleation of PbI_2 and the formation of complex iodoplumbate intermediates[39] (see Figure S5, Supporting Information) during gas quenching,[39] consistent with the XRD pattern of the films after gas quenching (see Figure 1b). These species are also observed in case of no additive or GACl, FACl, and KCl additive (see Figure S4, Supporting Information), indicating that they are thermodynamically favorable in nucleation. It is also shown that in the absence of the nucleation of α-phase perovskite, converting these species into α-phase perovskite is still possible through subsequent thermal annealing, but the resulting films suffer from inferior crystallinity and rapid phase degradation. We conclude thus far that when blade coating perovskite films from a $FAPbI_3$ precursor ink, the formation of a highly crystalline, stable α-$FAPbI_3$ film after thermal annealing is directly related to the room-temperature nucleation of α-phase nanocrystals during the gas-quenching stage. The growth of α-$FAPbI_3$ film during thermal annealing is highly likely templated by the α-phase nanocrystals formed before thermal annealing. Despite the nucleation of non-perovskite species upon the wet film's being supersaturated by gas quenching, nucleation of α-$FAPbI_3$ does not take place until CsCl or MACl is added into the $FAPbI_3$ precursor ink.

2.2. The Role of Cs in Nucleation

Having shown the critical role of CsCl in controlling the nucleation of α-$FAPbI_3$, it is imperative to consider whether Cs is alloyed into $FAPbI_3$ during film crystallization. The diffraction peak of the (200) planes of α-$FAPbI_3$, **Figure 2a**, shows a small but visible shift from 28.2° to 28.3° when CsCl is used as an additive, indicating a reduction of the lattice parameter by 0.0139 Å in the out-of-plane direction. Steady-state PL spectra, Figure 2b, show a ≈22-fold increase of intensity as CsCl is added, and more importantly, a shift of the emission peak by 18 nm toward a lower wavelength compared to the film prepared without CsCl. Figure S6 (Supporting Information) shows the UV–vis absorption spectra of the investigated thin films. The Tauc plots of the UV–vis absorption spectra,[40,41] Figure 2c, show a minor but noticeable increase in the optical bandgap from 1.52 to 1.54 eV when CsCl is added. The decrease of lattice spacing and the increase of bandgap both strongly suggest the incorporation of Cs into the $FAPbI_3$ lattice, forming eventually a $FA_{1-x}Cs_xPbI_3$ perovskite alloy ($0 < x \leq 0.1$). In the case of $FAPbI_3$ processed with CsCl additive, the (200) plane of the gas quenched film and the thermally annealed film show nearly identical peak positions of 28.27°, Figure 2d, despite a broadening of the XRD peak due to smaller crystal size before annealing.[42] It shows that these films have the same lattice constant, and thus we conclude that Cs is indeed alloyed into $FAPbI_3$ during the nucleation stage forming $FA_{1-x}Cs_xPbI_3$ nanocrystals.

The alloying of Cs into $FAPbI_3$ can be further evidenced by the progressive shift of the (100) and (200) peaks toward higher angles, Figure S7 and Table S2 (Supporting Information), by adding 5, 10, and 15% mol of excessive CsCl, showing that the

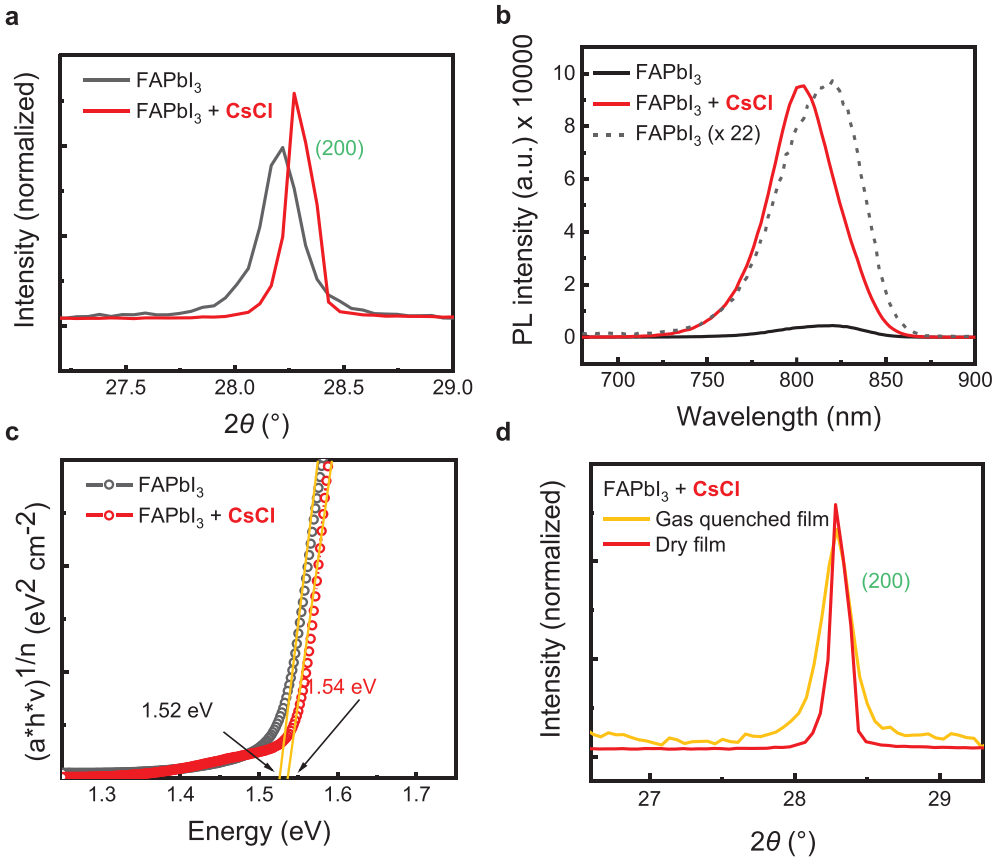

Figure 2. The role of Cs in the crystallization of α-$FAPbI_3$. a) XRD patterns of the (200) peak of $FAPbI_3$ film and FAPbI3 film with CsCl additive. b) Steady-state PL spectra of $FAPbI_3$ film and $FAPbI_3$ film with CsCl additive. The dashed line is the PL spectra of $FAPbI_3$ normalized to the same intensity as the spectra of $FAPbI_3$ + CsCl. c) Tauc plot of $FAPbI_3$ film and $FAPbI_3$ film with CsCl additive. d) XRD patterns of the (200) peak of $FAPbI_3$ film with CsCl additive after gas quenching and after thermal annealing.

nominal "additives" have a direct impact on the crystallization of perovskite films. In addition, increasing the amount of CsCl additive progressively increases the grain size in the resulting films (Figure S8, Supporting Information). The film processed with + 10% CsCl shows the best photovoltaic performance in the solar cells (Figure S9, Supporting Information), correlating to its highest PL intensity (Figure S10a, Supporting Information) and the slowest charge carrier decay (Figure S10b, Supporting Information), as measured by time-resolved PL (TRPL). The carrier lifetimes are estimated by fitting the TRPL curves with a bi-exponential decay model (details in Experimental Section) and the fitting parameters are listed in Table S3 (Supporting Information). It is found that the trend of average lifetime (τ_{av}) is consistent with the PL intensity. The τ_{av} reaches the longest time when 10% mol CsCl is added, increasing from 91.3 ns ($FAPbI_3$) to 324.8 ns. The greatly prolonged lifetimes indicate suppressed nonradiative recombination in the perovskite thin films. However, when the concentration further increases to 15% mol, the lifetimes decrease to 196.3 ns, which may be attributed to the phase separation occurring in perovskite films containing high concentrations of Cs.

In addition, no noticeable trace of Cl is found in the resulting film, at least on the surface, according to energy dispersive spectroscopic (EDS) analysis, Figure S11 (Supporting Information). It is highly likely that the residual FACl mostly sublimes from the film during the 150 °C thermal annealing.[43] We, therefore, conclude that despite being used as processing "additive", Cs has been incorporated in both the nuclei and the final film as alloys, forming Cs-FA "mix-cation" perovskite. Cs alloying is a critical factor driving the nucleation of α-$FAPbI_3$, a process that is thermodynamically favorable regardless of whether gas treatment is applied to the wet film (Figure S12, Supporting Information). The as-nucleated nanocrystals serve as templates to the growth of α-$FAPbI_3$ crystals, indispensable to obtaining crystalline, stable, and phase-pure films.

2.3. The Role of Cl in Crystal Growth

Having shown the indispensable role of Cs alloying in the nucleation of α-$FAPbI_3$, we then turn to investigate the role of Cl in enhancing the growth of the as-nucleated crystals and to demonstrate the universal mechanism behind the processing-additive strategy. In this regard, we investigate the films processed from inks with different precursor compositions: pure $FAPbI_3$ (referred to as "FA"), $FA_{0.9}Cs_{0.1}PbI_3$ ("CsFA"), $FAPbI_3$ with 10% mol CsCl additive ("FA+CsCl") and $FA_{0.9}Cs_{0.1}PbI_3$ with 10% mol FACl additive ("CsFA+FACl"). Surface scanning electron

microscopic (SEM) images, **Figure 3a**, show an increase in the lateral grain size for films containing Cl, namely both "FA + CsCl" and "CsFA + FACl" films, as compared to "CsFA" film. The films with CsCl or FACl additives also show lower surface roughness as observed from Haze measurements shown in Figure 3b. XRD patterns of these films, Figure 3c, show that phase-pure α-$FAPbI_3$ is obtained in all cases where Cs has been added to the precursor solution. However, the patterns show sharper and more intense diffraction peaks for "FA + CsCl" and "CsFA + FACl" films as compared to "CsFA" film, which is in good agreement with the increase of grain size observed from the surface SEM images. The statistical data of power conversion efficiency (PCE) of the solar cells, Figure 3d and Figure S8 (Supporting Information) show that "FA + CsCl" and "CsFA + FACl" exhibit comparable power conversion efficiencies (PCE), which are both higher than that of "CsFA". The results suggest that the addition of Cl leads to larger crystal size and higher film crystallinity, leading to improved optoelectronic qualities of the obtained perovskite films.

We then turn to the in-situ measurements to investigate the role of Cl by comparing the crystallization kinetics of "CsFA" and "CsFA + FACl" precursor inks. The evolution of PL during gas quenching is shown in Figure 3e,f, from which a couple of observations can be made: First, PL signals are observed in both cases of "CsFA" and "CsFA + FACl" upon turning on gas quenching, but "CsFA + FACl" shows a remarkably accelerated redshift of the PL peaks compared to "CsFA" during gas quenching. Second, "CsFA + FACl" shows a sharper rise of absorbance than "CsFA" during gas quenching and thus higher absorbance at the end of gas quenching, Figure 3g. The results first reaffirm our hypothesis stated above that Cs is indispensable to the nucleation of α-$FAPbI_3$. Second, the presence of Cl further enhances the growth of the as-nucleated nanocrystals during the gas quenching, such that larger crystals are formed prior to the thermal annealing of these films.

The chemical origin behind the acceleration of crystal growth by Cl ions, we postulate, is the stronger binding of Pb^{2+} with Cl^- than with I^-. We have found that the non-perovskite phase is a mixture of the so-called intermediate phase and δ-$FAPbI_3$ (Figure 1b,c). The interaction between Cl^- and Pb^{2+} on the one hand helps to break up the layered structure of PbI_2, thus accelerating the transition of PbI_2 to the intermediate phase,[44,45] and eventually the formation of the perovskite phase. On the other hand, the interaction of Cl^- with the Pb^{2+} is also reported to drive the δ-to-α phase transition.[7,46] In both cases, the growth of the α-$FAPbI_3$ nanocrystals can be accelerated.

We summarize in Figure 3h a universal thin-film formation mechanism of α-$FAPbI_3$ prepared with a scalable gas-quenching-assisted blade coating method: First, nucleation of perovskite phase during gas quenching, namely the emergence of α-$FAPbI_3$ nanocrystals and their subsequent growth, templates the growth of α-$FAPbI_3$ crystals during thermal annealing, which remains a key factor for the formation of crystalline and stable films after thermal annealing. In the absence of templated growth, α-$FAPbI_3$ can still be formed by thermal annealing the non-perovskite species but the obtained film remains highly unstable when cooling down to room temperature. Second, Cs is alloyed to $FAPbI_3$ during the nucleation stage, key to driving the formation of α-$FAPbI_3$ nanocrystals at room temperature. Third, Cl additive kinetically enhances crystal growth, leading to large crystals/grains and improved film crystallinity, but does not noticeably remain in the film after thermal annealing. A detailed understanding of the mechanism of "templated growth" during thermal annealing, as well as why it is more stable than the film obtained in its absence, requires a follow-up investigation employing x-ray-based in-situ techniques. However, our insights into the film growth enable us to formulate the precursor ink containing stoichiometric $FAPbI_3$ and CsCl additive that represents a reliable formula for the printing of phase-pure, highly crystalline, and stable α-$FAPbI_3$ thin films and thus provides a wide processing window for large scale production of perovskite PV devices.

2.4. Device Performance and Stability

To evaluate the photovoltaic performance of perovskite films prepared from the precursor ink that contains CsCl additive, we fabricated perovskite solar cells (PSC) with an architecture of ITO/SnO_2/perovskite/TaTm/PEDOT/Carbon. Indium-doped tin oxide (ITO) is the bottom contact, tin oxide (SnO_2) is the electron transporting layer, a bilayer of N4,N4,N4,00N400-tetra([1,10-biphenyl]-4-yl)-[1,10:40100-terphenyl]-4400-diamine (TaTm) and poly(3,4-ethylenedioxythiophene):polystyrene sulfonate (PEDOT:PSS) is used as hole transporting layer, carbon is used as the top electrode. All layers are fabricated by printing method under ambient conditions with controlled relative humidity (<10% RH). **Figure 4a** shows the current density–voltage (*J–V*) curves of the champion solar cells processed from perovskite films with 10 mol% CsCl additive, which shows a short-circuit current density (J_{SC}) of 24.47 mA cm^{-2}, an open-circuit voltage (V_{OC}) of 1.08 V, a fill factor (FF) of 73.27% and a PCE of 19.36%, measured from the reverse JV scan (i.e., open circuit to short circuit). As a reference, metal-electrode devices are prepared with an architecture of ITO/SnO_2/perovskite/PDCBT/Ta-WO_X/Au, in which PDCBT is Poly[2,2″-bis[[(2-butyloctyl)oxy]carbonyl]-[2,2′:5′,2″:5″,2″-quaterthiophene]-5,5″-diyl] and Ta-WO_x is tantalum doped tungsten oxide. The SnO_2 and perovskite layers are blade-coated, while PDCBT and Ta-WO_x are spin-coated and the gold electrode is thermally evaporated. The champion cell shows J_{SC} of 25.24 mA cm^{-2}, V_{OC} of 1.13 V, FF of 76.11%, and PCE values of 21.71% measured from the reverse-scan JV curve.

It is also seen from Figure 4a that the PSC with Au electrode (Au-PSC) shows negligible JV hysteresis whilst the carbon-PSC shows a more expressed hysteresis, which is probably caused by the accumulation of charges at the HTL/carbon interface.[47] We, therefore, determined the stabilized power output (SPO) by measuring the time-dependent photocurrent and the corresponding PCE at the voltage (V_{MPP}) near the maximum power point (MPP), Figure 4b, which shows a steady-state PCE of 19.10% for the C-PSCs and a 21.42% for the Au-PSCs. The external quantum efficiency (EQE) spectra of the devices are shown in Figure 4c and Figure S13 (Supporting Information). The corresponding integrated J_{SC} values of 23.27 and 24.44 mA cm^{-2} obtained from the EQE spectra of the C-PSCs and Au-PSCs, respectively, are in good agreement with the J_{SC} measured by *J–V* characterization. The Au-PSCs exhibit a somewhat higher J_{SC} than the C-PSCs within the wavelength range of 500 to 800 nm. This discrepancy is attributed to the diminished optical

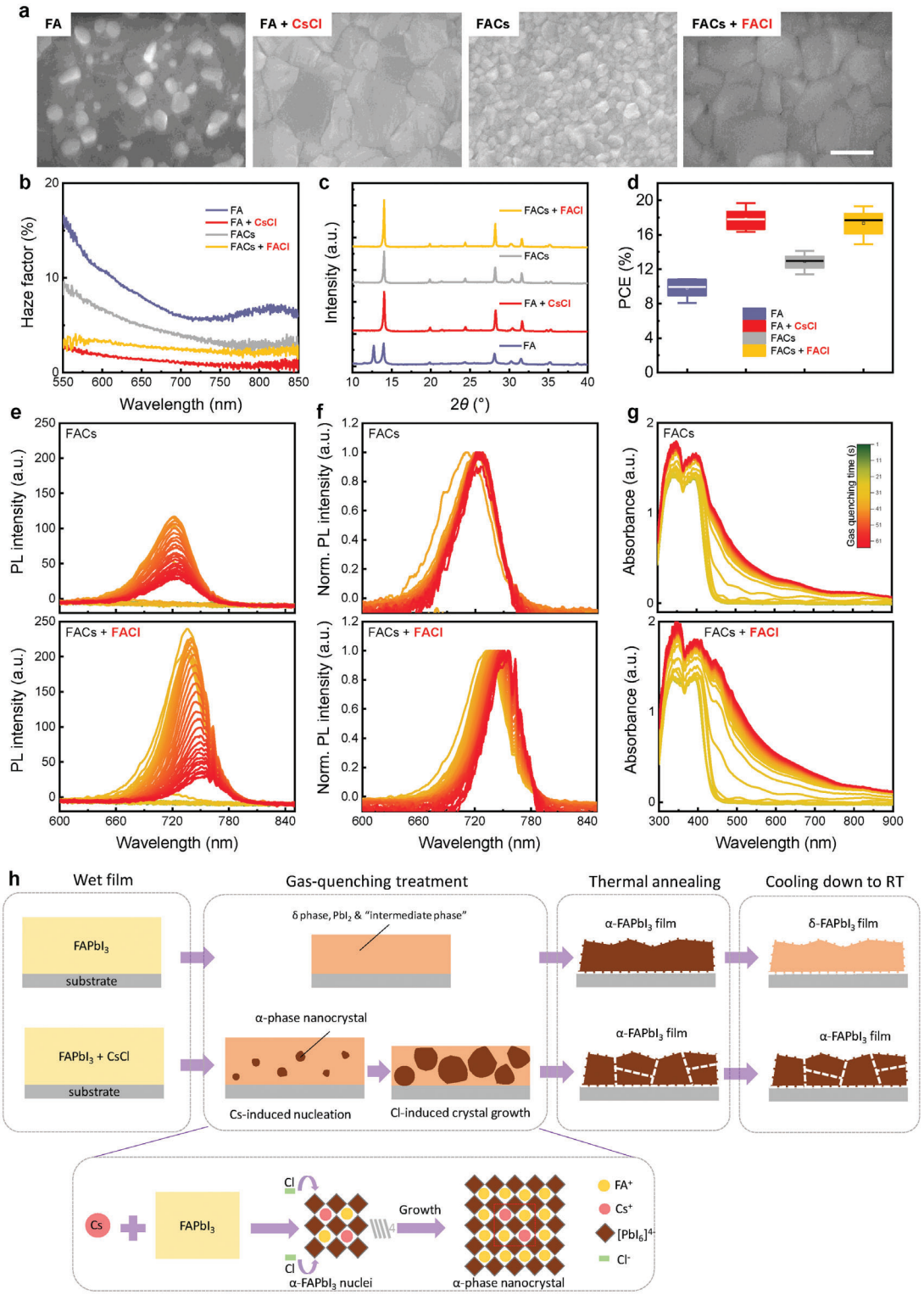

Figure 3. The role of Cl in the crystallization of α-$FAPbI_3$. a) Surface SEM images of the annealed films processed from precursor inks containing four categories of precursors: pure $FAPbI_3$ ("FA"), $FAPbI_3$ with CsCl additive ("FA+CsCl"), $FA_{0.9}Cs_{0.1}PbI_3$ ("FACs") and $FA_{0.9}Cs_{0.1}PbI_3$ with FACl additive ("FACs+FACl"). The scale bar is 500 nm. b) Transmission haze spectra of the annealed perovskite films. c) XRD patterns of the FA, FA+CsCl, FACs, and FACs + FACl films. d) Statistical data of PCE of solar cells containing different FA-based perovskite films, measured from 30 cells for each condition. e) Evolution of the PL spectra of "FACs" film and "FACs + FACl" film during gas quenching treatment. f) Normalized spectra of the PL evolution. g) Evolution of the absorption spectra of "FACs" film and "FACs + FACl" film during gas quenching treatment. h) Schematic drawing of the role of CsCl in the nucleation, crystal growth, and film formation of α-$FAPbI_3$.

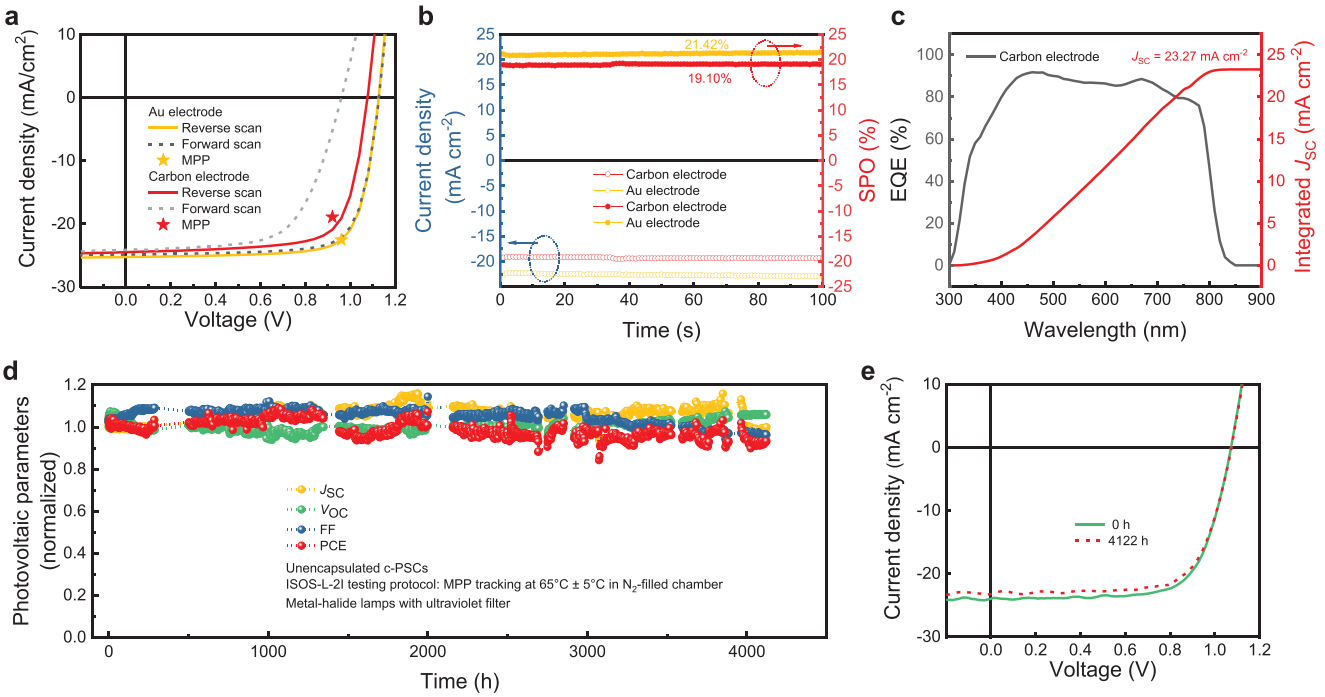

Figure 4. Photovoltaic performance and operation stability of solar cells. a) *J–V* curves of the champion PSCs with carbon and gold electrodes, measured with both forward scan and reverse scan at 50 mV s^{-1}. The stars indicate the MPP of the two PSCs at which stabilized PCEs are measured. b) Time-dependent photocurrent and PCE at the MPP of the champion C-PSC and champion Au-PSC. c) EQE spectra champion C-PSC. d) The evolution of photovoltaic parameters normalized to the initial values of C-PSCs, aging under continuous illumination of 1 sun equivalent irradiation at 65 °C in a nitrogen atmosphere. e) Reverse-scan J–V curves of a C-PSC before and after aging of 4122 h.

losses resulting from the high reflectance of the Au electrode in the spectral range of non-saturated absorption by the perovskite layer.

Operational stability of the perovskite film prepared with our CsCl-additive strategy is examined by measuring the evolution of PCE and other photovoltaic (PV) parameters of the C-PSCs at 65 ± 5 °C under 1 sun equivalent illumination in a nitrogen atmosphere. As Figure 4d shows, the unencapsulated C-PSC maintains 95% of its initial PCE during the aging test (maximum power point tracking mode). The *J–V* curves of a device measured before and after operation for 4,122 h, Figure 4e, are almost identical. These observations confirm that the incorporation of CsCl in the preparation of high-quality $FAPbI_3$ films provides exceptional long-term stability.

2.5. Solar Module Performance and Stability

Upscaling fabrication of the perovskite film is actively pursued in the way of realizing practical applications of perovskite photovoltaic technologies. We therefore fabricated perovskite mini solar modules on a 5 cm × 5 cm substrate, with seven cells monolithically interconnected in series and a shim-coated carbon top electrode to demonstrate the scalability of the CsCl-additive strategy. To underline the significance of this work, **Figure 5a** compares the efficiency versus area of the state-of-the-art C-PSMs. The detailed photovoltaic parameters are summarized in Table S4 (Supporting Information). It is worthwhile noting that our work presents low-temperature processed carbon electrodes on a fully printed planar configuration with ambient processibility, which is potentially transferable to high-throughput roll-to-roll production.

Figure 5b shows the schematic drawing of the interconnection of the individual cells within the C-PSM. The serial interconnection of the module was realized by P1, P2, and P3 lines. The P1 and P2 lines were patterned by laser ablation, whereas the P3 line was fabricated with a tape mask when printing the carbon electrode. Figure 5c plots the *J–V* curve of the champion module, which shows a PCE of 16.67%, with active area J_{SC} of 23.09 mA cm^{-2}, V_{OC} per unit cell of 1.00 V, and FF of 72.18% (reverse scan). We measured the time-dependent photocurrent and the corresponding PCE at the voltage near MPP. The photocurrent at the MPP is shown in Figure 5d, yielding a stabilized PCE of 16.23%. To the best of our knowledge, this is by far the highest value of stabilized PCE for fully printed C-PSMs.[48]

Lastly, we evaluate the environmental stability of a C-PSM encapsulated with polyisobutylene (PIB) sealant on the edges and a cover glass on the top (Figure S14, Supporting Information).[49] The C-PSMs were then subjected to the International Electrotechnical Commission (IEC) 61 215:2021 damp heat test carried out at 85 °C and 85% relative humidity in an environmental chamber. Figure 5e and Figure S15 (Supporting Information) show the evolution of the *J–V* parameters of the encapsulated and non-encapsulated c-PSMs. The encapsulated C-PSM experienced no degradation after 700 h damp heat exposure, whereas non-encapsulated C-PSM died within a few hours. These results

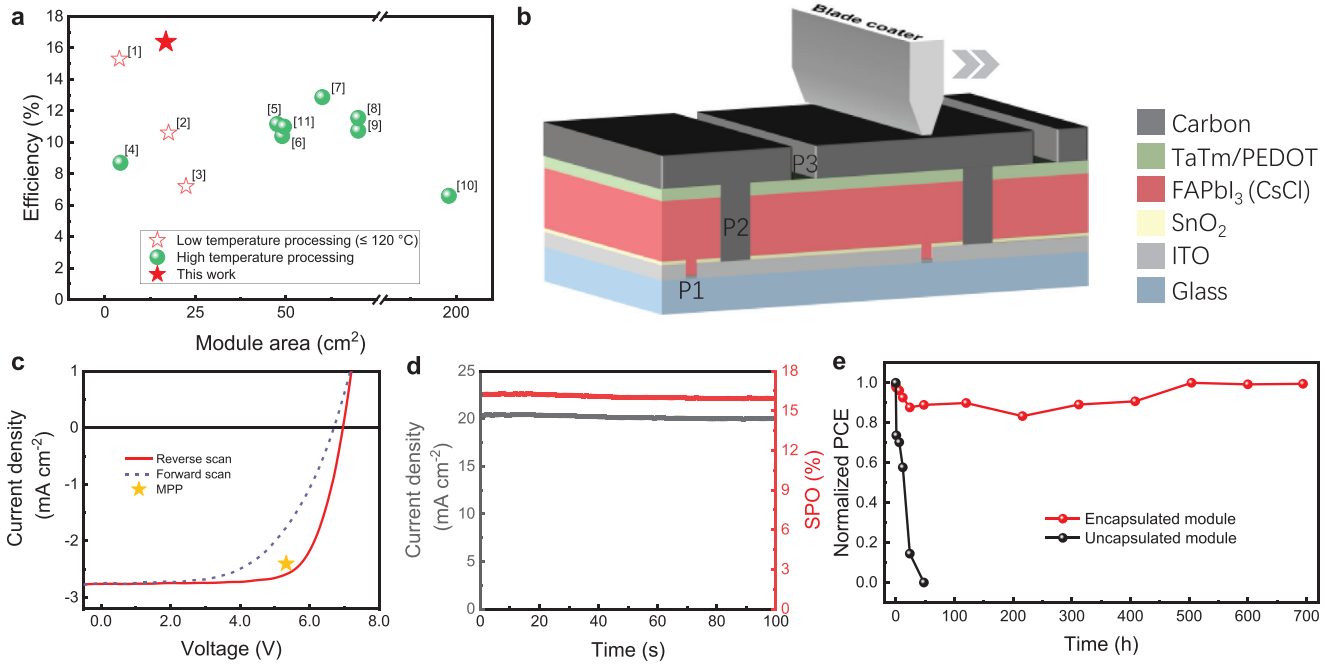

Figure 5. Photovoltaic performance and damp heat stability of solar mini-modules. a) Summary of PCE versus active area of previously reported perovskite solar modules with carbon electrode. b) Schematic drawing of the fully printed perovskite mini-module with carbon electrode. c) *J–V* curves of the champion mini-module with an aperture area of 20.25 cm^2 and active area of 16.84 cm^2. The star indicates the stabilized maximum power point. d) Time-dependent photocurrent and PCE at the MPP (SPO). e) Evolution of PCE of an encapsulated and an unencapsulated C-PSM in damp-heat testing (85 °C and 85% relative humidity).

show the satisfactory stability of the printed perovskite films under elevated temperatures and that a simple edge encapsulation can effectively protect the solar module against harsh moisture/temperature exposure.

3. Conclusion

In conclusion, we investigated the formation mechanism of $FAPbI_3$ perovskite film prepared by gas-quenching-assisted blade coating via in situ optical techniques. We demonstrated an additive-engineering strategy by incorporating CsCl to $FAPbI_3$ precursor to be effective and reliable in controlling α-$FAPbI_3$ crystallization. The key findings evidence a two-step mechanism: Cs is essential in promoting the formation of α-phase FA-Cs nucleation centers when the film is supersaturated, while Cl plays a critical role in increasing the growth rate of the nanocrystals. We further unravel that Cs is alloyed into $FAPbI_3$ since the nucleation stage and remains present in the resulting crystalline film even after annealing, whereas no chloride is found in the final films. Understanding the role of the respective ionic species allows for generalization of the additive engineering, that the precursor ink formula of "$FAPbI_3$ with CsCl additive" is essentially equivalent to a mixed-cation formula of "$Cs_xFA_{1-x}PbI_3$ with FACl additive", both resulting in high-quality $FA_xCs_{1-x}PbI_3$ ($0 < x \leq 0.1$) perovskite films. These films are turned into fully printed C-PSCs with a promising PCE of 19.36%. Replacing the carbon electrode with an Au-electrode further increases the cell efficiency to 21.71%. Additionally, the carbon electrode-based mini-modules with an aperture area of 20.25 cm^2 delivered a champion stabilized PCE of up to 16.23%. We further demonstrated impressive operational stability for the unencapsulated C-PSCs for 4,122 h under 65 °C in N_2 atmosphere and under 1 sun illumination from metal-halide lamps. PIB encapsulated c-PSM sustained 700 h damp heat testing (85% RH, 85 °C) without degradation. This study provides a universal route to print the black and stable-phase $FAPbI_3$ film for stable fully printed perovskite PV.

Supporting Information

Supporting Information is available from the Wiley Online Library or from the author.

Acknowledgements

The authors acknowledge financial support from the Bavarian State Government (FKZ 20.2-3410.5-4-5). Research has also been carried out at the "Solar Factory of the Future", an initiative under the cooperation between FAU (i-MEET) and FZJ (HI ERN) that is located at the Energy Campus Nürnberg (EnCN). We further acknowledge the financial support from Deutsche Forschungsgemeinschaft (DFG) via the Perovskite SPP2196 program (Project NO. 506698391). Part of this work has been supported by the Helmholtz Association in the framework of the innovation platform "Solar TAP". F.Y. acknowledges the financial support from the National Natural Science Foundation of China (Grant Nos. 52102287), the Natural Science Foundation of Jiangsu Province (Grant No. BK20210731), the Natural Science Foundation of the Jiangsu Higher Education Institutions of China (21KJD150003). S.Q., Z.X., C.L., and J.L. acknowledge the support from the China Scholarship Council (CSC).

Open access funding enabled and organized by Projekt DEAL.

Conflict of Interest

The authors declare no conflict of interest.

Author Contributions

S.Q., F.Y., T.D., C.J.B., and H.-J.E. conceived the idea and designed the experiments. S.Q. carried out the preparation of perovskite film and device fabrication. S.Q. carried out film characterization, device characterization, and optical and photoluminescence measurements. S.Q. and D.J. carried out in situ PL and UV–vis absorption measurements. L.D. and T.D. conducted optimization of charge transport layers. J.G.C. conducted the design of the module layout. S.Q. and Z.X. carried out the EDS measurements. J.L. and C.L. carried out the gold-electrode evaporation. All authors discussed the results and commented on the manuscript. C.J.B., T.D. and H.-J.E. directed and supervised the entire research.

Data Availability Statement

The data that support the findings of this study are available from the corresponding author upon reasonable request.

Keywords

carbon-electrode, cesium ion, $FAPbI_3$, nucleation, perovskite photovoltaics

Received: June 16, 2024
Revised: September 4, 2024
Published online: October 8, 2024

[1] H. Min, M. Kim, S.-U. Lee, H. Kim, G. Kim, K. Choi, J. H. Lee, S. Il. Seok, *Science (1979)* **2019**, *366*, 749.
[2] G. E. Eperon, S. D. Stranks, C. Menelaou, M. B. Johnston, L. M. Herz, H. J. Snaith, *Energy Environ Sci.* **2014**, *7*, 982.
[3] K. Wang, W. S. Subhani, Y. Wang, X. Zuo, H. Wang, L. Duan, S. Liu, *Adv. Mater.* **2019**, *31*, 1902037.
[4] Z. Wang, Z. Shi, T. Li, Y. Chen, W. Huang, *Angew. Chem.* **2017**, *56*, 1190.
[5] J. Jeong, M. Kim, J. Seo, H. Lu, P. Ahlawat, A. Mishra, Y. Yang, M. A. Hope, F. T. Eickemeyer, M. Kim, Y. J. Yoon, I. W. Choi, B. P. Darwich, S. J. Choi, Y. Jo, J. H. Lee, B. Walker, S. M. Zakeeruddin, L. Emsley, U. Rothlisberger, A. Hagfeldt, D. S. Kim, M. Grätzel, J. Y. Kim, *Nature* **2021**, *592*, 381.
[6] H. Chen, Y. Chen, T. Zhang, X. Liu, X. Wang, Y. Zhao, *Small Struct.* **2021**, *2*, 2000130.
[7] H. Lu, Y. Liu, P. Ahlawat, A. Mishra, W. R. Tress, F. T. Eickemeyer, Y. Yang, F. Fu, Z. Wang, C. E. Avalos, B. I. Carlsen, A. Agarwalla, X. Zhang, X. Li, Y. Zhang, S. M. Zakeeruddin, L. Emsley, U. Rothlisberger, L. Zheng, A. Hagfeldt, M. Grätzel, *Science (1979)* **2020**, *370*, eabb8985.
[8] S.-Y. Ju, W. I. Lee, H.-S. Kim, *ACS Appl. Mater. Interfaces* **2022**, *14*, 39996.
[9] X. Cui, J. Jin, Q. Tai, F. Yan, *Sol. RRL* **2022**, *6*, 2200497.
[10] J. W. Yoo, E. Noh, J. Jang, K. S. Lee, J. Byeon, M. Choi, J. Im, S. Il. Seok, *Joule* **2023**, *7*, 797.
[11] X. Dong, L. Chao, T. Niu, Y. Li, P. Guo, W. Hui, L. Song, Z. Wu, Y. Chen, *Sol. RRL* **2022**, *6*, 2200060.
[12] B.-W. Park, H. W. Kwon, Y. Lee, D. Y. Lee, M. G. Kim, G. Kim, K.-J. Kim, Y. K. Kim, J. Im, T. J. Shin, S. Il. Seok, *Nat. Energy* **2021**, *6*, 419.
[13] P. Shi, Y. Ding, B. Ding, Q. Xing, T. Kodalle, C. M. Sutter-Fella, I. Yavuz, C. Yao, W. Fan, J. Xu, Y. Tian, D. Gu, K. Zhao, S. Tan, X. Zhang, L. Yao, P. J. Dyson, J. L. Slack, D. Yang, J. Xue, M. K. Nazeeruddin, Y. Yang, R. Wang, *Nature* **2023**, *620*, 323.
[14] S. Sánchez, S. Cacovich, G. Vidon, J.-F. Guillemoles, F. Eickemeyer, S. M. Zakeeruddin, J. E. K. Schawe, J. F. Löffler, C. Cayron, P. Schouwink, M. Grätzel, *Energy Environ Sci.* **2022**, *15*, 3862.
[15] J. Zhao, S. O. Fürer, D. P. McMeekin, Q. Lin, P. Lv, J. Ma, W. L. Tan, C. Wang, B. Tan, A. S. R. Chesman, H. Yin, A. D. Scully, C. R. McNeill, W. Mao, J. Lu, Y.-B. Cheng, U. Bach, *Energy Environ. Sci.* **2023**, *16*, 138.
[16] Y. Huang, X. Lei, T. He, Y. Jiang, M. Yuan, *Adv. Energy Mater.* **2022**, *12*, 2100690.
[17] S. Masi, A. F. Gualdrón-Reyes, I. Mora-Sero, *ACS Energy Lett.* **2020**, *5*, 1974.
[18] W. Feng, J. Tao, G. Liu, G. Yang, J.-X. Zhong, Y. Fang, L. Gong, S. Yang, W. Wu, *Angew. Chem.* **2023**, *62*, 202300265.
[19] X. Shen, B. M. Gallant, P. Holzhey, J. A. Smith, K. A. Elmestekawy, Z. Yuan, P. V. G. M. Rathnayake, S. Bernardi, A. Dasgupta, E. Kasparavicius, T. Malinauskas, P. Caprioglio, O. Shargaieva, Y.-H. Lin, M. M. McCarthy, E. Unger, V. Getautis, A. Widmer-Cooper, L. M. Herz, H. J. Snaith, *Adv. Mater.* **2023**, 2211742.
[20] H. T. Pham, Y. Yin, G. Andersson, K. J. Weber, T. Duong, J. Wong-Leung, *Nano Energy* **2021**, *87*, 106226.
[21] X. Liu, D. Luo, Z.-H. Lu, J. S. Yun, M. Saliba, S. Il. Seok, W. Zhang, *Nat. Rev. Chem.* **2023**, *7*, 462.
[22] S. Shin, S. Seo, S. Jeong, A. S. Sharbirin, J. Kim, H. Ahn, N. Park, H. Shin, *Adv. Sci.* **2023**, 2300798.
[23] F. Yang, D. Jang, L. Dong, S. Qiu, A. Distler, N. Li, C. J. Brabec, H.-J. Egelhaaf, *Adv. Energy Mater.* **2021**, *11*, 202101973.
[24] N.-G. Park, K. Zhu, *Nat. Rev. Mater.* **2020**, *5*, 333.
[25] Y. Tang, Z. Gu, C. Fu, Q. Xiao, S. Zhang, Y. Zhang, Y. Song, *Sol. RRL* **2022**, *6*, 2200120.
[26] F. Guo, S. Qiu, J. Hu, H. Wang, B. Cai, J. Li, X. Yuan, X. Liu, K. Forberich, C. J. Brabec, Y. Mai, *Adv. Sci.* **2019**, *6*, 201901067.
[27] Z. Saki, M. M. Byranvand, N. Taghavinia, M. Kedia, M. Saliba, *Energy Environ. Sci.* **2021**, *14*, 5690.
[28] H. C. Weerasinghe, N. Macadam, J.-E. Kim, L. J. Sutherland, D. Angmo, L. W. T. Ng, A. D. Scully, F. Glenn, R. Chantler, N. L. Chang, M. Dehghanimadvar, L. Shi, A. W. Ho-Baillie, R. Egan, A. S. R. Cheman, M. Gao, J. J. Jasieniak, T. Hasan, D. Vak, *Nat. Commun.* **2024**, *15*, 1656.
[29] Y. Yu, F. Zhang, T. Hou, X. Sun, H. Yu, M. Zhang, *Sol. RRL* **2021**, *5*, 2100386.
[30] W. Xiang, J. Zhang, S. F. Liu, S. Albrecht, A. Hagfeldt, Z. Wang, *Joule* **2022**, *6*, 315.
[31] Y. Zhou, Z. Guo, S. M. H. Qaid, Z. Xu, Y. Zhou, Z. Zang, *Sol. RRL* **2023**, *7*, 2300438.
[32] T. Bu, J. Li, H. Li, C. Tian, J. Su, G. Tong, L. K. Ono, C. Wang, Z. Lin, N. Chai, X.-L. Zhang, J. Chang, J. Lu, J. Zhong, W. Huang, Y. Qi, Y.-B. Cheng, F. Huang, *Science (1979)* **2021**, *372*, 1327.
[33] K. Park, S. Tan, T. Kodalle, D. Lee, M. Abdelsamie, J.-S. Park, J.-H. Lee, S.-K. Jung, J. H. Ko, N.-G. Park, C. M. Sutter-Fella, Y. Yang, J.-W. Lee, *Adv. Mater.* **2024**, *36*, 2307265.
[34] J. Park, J. Kim, H.-S. Yun, M. J. Paik, E. Noh, H. J. Mun, M. G. Kim, T. J. Shin, S. Il Seok, *Nature* **2023**, *616*, 724.
[35] L. Wagner, L. E. Mundt, G. Mathiazhagan, M. Mundus, M. C. Schubert, S. Mastroianni, U. Würfel, A. Hinsch, S. W. Glunz, *Sci. Rep.* **2017**, *7*, 14899.
[36] S. Qiu, M. Majewski, L. Dong, D. Jang, V. M. Le Corre, J. G. Cerrillo, O. J. J. Ronsin, F. Yang, F. Guo, K. Zhang, L. Lüer, J. Harting, T. Du, C. J. Brabec, H.-J. Egelhaaf, *Adv. Energy Mater.* **2024**, 2303210.
[37] S. Pratap, F. Babbe, N. S. Barchi, Z. Yuan, T. Luong, Z. Haber, T.-B. Song, J. L. Slack, C. V. Stan, N. Tamura, C. M. Sutter-Fella, P. Müller-Buschbaum, *Nat. Commun.* **2021**, *12*, 5624.

[38] D.-K. Lee, Y. Shin, H. J. Jang, J.-H. Lee, K. Park, W. Lee, S. Yoo, J. Y. Lee, D. Kim, J.-W. Lee, N.-G. Park, *ACS Energy Lett.* **2021**, *6*, 1821.
[39] E. Radicchi, E. Mosconi, F. Elisei, F. Nunzi, F. De Angelis, *ACS Appl. Energy Mater.* **2019**, *2*, 3400.
[40] D. H. Yeon, S. M. Lee, Y. H. Jo, J. Moon, Y. S. Cho, *J. Mater. Chem. A* **2014**, *2*, 20112.
[41] O. Almora, C. I. Cabrera, J. Garcia-Cerrillo, T. Kirchartz, U. Rau, C. J. Brabec, *Adv. Energy Mater.* **2021**, *11*, 2100022.
[42] J. T.-W. Wang, Z. Wang, S. Pathak, W. Zhang, D. W. deQuilettes, F. Wisnivesky-Rocca-Rivarola, J. Huang, P. K. Nayak, J. B. Patel, H. A. M. Yusof, Y. Vaynzof, R. Zhu, I. Ramirez, J. Zhang, C. Ducati, C. Grovenor, M. B. Johnston, D. S. Ginger, R. J. Nicholas, H. J. Snaith, *Energy Environ. Sci.* **2016**, *9*, 2892.
[43] M. M. Tavakoli, P. Yadav, D. Prochowicz, M. Sponseller, A. Osherov, V. Bulović, J. Kong, *Adv. Energy Mater.* **2019**, *9*, 1803587.
[44] B. Li, M. Li, C. Fei, G. Cao, J. Tian, *J. Mater. Chem. A* **2017**, *5*, 24168.
[45] M. Kim, G.-H. Kim, T. K. Lee, I. W. Choi, H. W. Choi, Y. Jo, Y. J. Yoon, J. W. Kim, J. Lee, D. Huh, H. Lee, S. K. Kwak, J. Y. Kim, D. S. Kim, *Joule* **2019**, *3*, 2179.
[46] T. Du, T. J. Macdonald, R. X. Yang, M. Li, Z. Jiang, L. Mohan, W. Xu, Z. Su, X. Gao, R. Whiteley, C.-T. Lin, G. Min, S. A. Haque, J. R. Durrant, K. A. Persson, M. A. McLachlan, J. Briscoe, *Adv. Mater.* **2022**, *34*, 2107850.
[47] Y. Rong, Y. Hu, S. Ravishankar, H. Liu, X. Hou, Y. Sheng, A. Mei, Q. Wang, D. Li, M. Xu, J. Bisquert, *Energy Environ. Sci.* **2017**, *10*, 2383.
[48] M. Stefanelli, L. Vesce, A. Di Carlo, *Nanomaterials* **2023**, *13*, 313.
[49] L. Shi, M. P. Bucknall, T. L. Young, M. Zhang, L. Hu, J. Bing, D. S. Lee, J. Kim, T. Wu, N. Takamure, D. R. Mckenzie, S. Huang, M. A. Green, A. W. Y. Yo-Baillie, *Science (1979)* **2020**, *368*, eaba2412.